Draft version July 22, 2021
Preprint typeset using LaTeX style emulateapj v. 5/2/11

SUPERMASSIVE BLACK HOLES IN GALACTIC NUCLEI WITH TIDAL DISRUPTION OF STARS: PAPER II - AXISYMMETRIC NUCLEI

Shiyan Zhong [1], Peter Berczik [1,2,3], Rainer Spurzem [1,2,4,5]

Draft version July 22, 2021

Abstract

Tidal Disruption of stars by supermassive central black holes from dense rotating star clusters is modelled by high-accuracy direct N-body simulation. As in a previous paper on spherical star clusters we study the time evolution of the stellar tidal disruption rate and the origin of tidally disrupted stars, now according to several classes of orbits which only occur in axisymmetric systems (short axis tube and saucer). Compared with that in spherical systems, we found a higher TD rate in axisymmetric systems. The enhancement can be explained by an enlarged loss-cone in phase space which is raised from the fact that total angular momentum **J** is not conserved. As in the case of spherical systems, the distribution of the last apocenter distance of tidally accreted stars peaks at the classical critical radius. However, the angular distribution of the origin of the accreted stars reveals interesting features. Inside the influence radius of the supermassive black hole the angular distribution of disrupted stars has a conspicuous bimodal structure with a local minimum near the equatorial plane. Outside the influence radius this dependence is weak. We show that the bimodal structure of orbital parameters can be explained by the presence of two families of regular orbits, namely short axis tube and saucer orbits. Also the consequences of our results for the loss cone in axisymmetric galactic nuclei are presented.

Subject headings: black holes – galactic nuclei – stellar dynamics

1. INTRODUCTION

A large fraction of galaxies show evidence of supermassive black holes (henceforth SMBH) residing in their center. They are typically embedded in nuclear star clusters (NSC); if resolution allows to observe the NSCs, they are among the densest clusters known. Their size is similar to galactic globular clusters, but they are much heavier and brighter (Böker et al. 2002, 2004). In massive galaxies NSCs may not be significant or even do not exist, however, the SMBHs are still surrounded by enormous number of stars. SMBH residing in these NSCs will tidally disrupt stars that come close to its tidal radius and eventually accrete the gaseous debris, which can light up the central SMBH for a period of time (Rees 1988; Evans & Kochanek 1989). This kind of event is a useful tool to examine the relativistic physics near SMBH since the disruption occurs at a place very close to the BH's Schwarzschild radius. Also it can help us to investigate SMBH in non-active galactic center. Although tidal disruption of stars has been proposed for almost half a century, only until last decade do people realize the importance of such events, after the discovery of a dozens of tidal disruption candidates (Komossa 2002; Komossa & Merritt 2008). Liu et al. (2014) discovered a candidate of binary SMBH system by analyzing the break in the light curve of TD event, demonstrate it as a promising tool for searching hidden SMBH binaries in quiescent galactic center. In order to compute the tidal disruption event rate, many theoretic works have been done in the past few decades (Frank & Rees 1976; Lightman & Shapiro 1977; Magorrian & Tremaine 1999; Wang & Merritt 2004). The core of the story is loss cone theory, which was first established in the case of spherical symmetric systems.

Stars with orbital pericenter smaller than the tidal radius r_t are defined to be inside the loss cone, with r_t be expressed by

$$r_t = \alpha r_\star \frac{3}{5-n}\left(\frac{M_{\rm bh}}{m_\star}\right)^{\frac{1}{3}} , \quad (1)$$

where $r_\star$, $m_\star$ are the radius and mass of a star, n is its polytropic index (assuming the stellar structure can be approximated by a polytropic sphere) and α is a free parameter used by us for scaling. Stars with angular momentum $J < J_{lc} \approx \sqrt{2GM_\bullet r_t}$ are inside the loss cone. Typically, loss cone stars are consumed in dynamical time scales. If no new star is supplied to loss cone, there will be no more tidal disruption event. Based on the status of loss cone, it can be divided into two regime, namely empty and full loss cone. Due to the short "lifetime" of the loss cone stars, loss cone will become empty quickly. Refilling of loss cone happens in relaxation timescales and is often referred to as diffusion process in angular momentum space. Thus in empty loss cone regime it is the refilling rate which controls the disruption rate. Note that throughout this paper, and like in most if not all of the cited papers on tidal accretion of stars onto SMBH, we assume that a star is disrupted completely at r_t and all its mass, energy and angular momentum absorbed momentarily by the SMBH. We

[1] National Astronomical Observatories of China and Key Lab for Computational Astrophysics, Chinese Academy of Sciences, 20A Datun Rd., Chaoyang District, 100012, Beijing, China
[2] Astronomisches Rechen-Institut, Zentrum für Astronomie, University of Heidelberg, Mönchhofstrasse 12-14, 69120, Heidelberg, Germany
[3] Main Astronomical Observatory, National Academy of Sciences of Ukraine, 27 Akademika Zabolotnoho St., 03680, Kyiv, Ukraine
[4] Kavli Institute for Astronomy and Astrophysics, Peking University, Beijing, China
[5] Key Lab of Frontiers in Theoretical Physics, Institute of Theoretical Physics, Chinese Academy of Sciences, Beijing, 100190, P.R. China

know that this is not realistic, and more detailed numerical models of the process of disruption, possible disk formation and accretion show that only fractions of the material are absorbed into the SMBH after a number of orbits (Guillochon & Ramirez-Ruiz 2013; Hayasaki et al. 2013). However, the assumption that the process is fast is reasonable compared to the orbital time scales of stars further out in the cluster.

In a previous paper (Zhong et al. (2014), henceforth Paper I) we have shown that the classical loss cone approximation, for a spherically symmetric system in the diffusive empty loss cone regime, can be well reproduced by large direct N-body models with tidal accretion of stars onto SMBH. Now we are focusing on the generalization to axisymmetric galactic nuclei and compare our new results in an otherwise very similar study to those of Paper I.

Tidal disruption of stars is one possible way of growth for SMBH, especially in quiescent galactic nuclei. Since most models assumed spherical stellar clusters, SMBH growth rates by tidal disruption are very low, limited by the very long relaxation time to refill the loss cone, and the contribution of the process to the overall growth of SMBH is considered as relatively insignificant. However, the stellar distribution in real galactic nuclei might not be spherically symmetric. Many galactic nuclei show evidence of rotation in their centers, even very close to the SMBH (Miyoshi et al. 1995; Neufeld & Maloney 1995; Greenhill et al. 1995).

According to the current standard model of structure formation massive galaxies have undergone quite significant mergers (in number and mass ratio). Numerical models of the merging process of galaxies show that the merger remnant shows rotation, axial symmetry or even triaxiality in the central regions (Khan et al. 2011; Preto et al. 2011; Gualandris & Merritt 2012; Bois et al. 2013).

In the center of our own Milky Way the NSC can be observed in unparalleled high resolution (Feldmeier et al. 2014; Schödel et al. 2014). It consists of $1.4 \times 10^7 M_\odot$ within its effective radius (4.2 pc); kinematic data indicate that it possesses bulk rotation (Feldmeier et al. 2014). The formation mechanism of NSCs is still under debate. There are two scenarios, *in situ* formation (Milosavljević 2004) and a sinking scenario (globular cluster sink to the center and merge) (Tremaine et al. 1975; Lotz et al. 2001). NSCs in a sample of nearby galaxies observed by Seth et al. (2006, 2008) show that these objects are non-spherical and even contain multicomponent (younger disk plus older spherical component),which favor the *in situ* scenario. However, Antonini et al. (2012) have performed a series of N-body simulations to study the formation of NSCs, which support the sinking scenario. The model NSCs formed in their simulations by merging between infalling globular clusters initially have mildly triaxial shape. After the final infall, the shape of the NSC will gradually become axisymmetric in following dynamical evolution.

Despite the debate between different formation scenarios, we think that it is quite likely that NSC are non-spherical. This provides a good motivation to study the tidal disruption rate in axisymmetric (and triaxial) clusters. Some works have already been done but the mission is not over. Fiestas & Spurzem (2010) used 2D Fokker-Plank model (Einsel & Spurzem 1999; Kim et al. 2002) to study rotating dense stellar clusters with BHs and cross checked with N-body models (Fiestas et al. 2012). Both works find that BH embedded in rotating model have higher tidal disruption rate (hereafter TDR) compare to spherical models. BH mass at the end of simulation is roughly 20% higher in rotating case. They find an excess of accreted prograde rotating stars which are originated mainly outside the influence radius r_h and call for a further investigation of the roles of stars with non-conserved J_x, J_y angular momentum. As shown by the works of Merritt & Poon (2004), in non-spherical systems chaotic orbits (existing in regions outside r_h) can keep the loss cone full for sufficient long time, thus tidal disruption can contribute a lot of mass within Hubble time and could play an important role in the BH growth across cosmic time.

On the other hand, the loss cone itself might be enlarged as pointed out by Magorrian & Tremaine (1999), due to the fact that angular momentum **J** is not conserved in axisymmetric potential. Vasiliev & Merritt (2013) confirmed this picture in a detailed analysis of the loss cone problem in axisymmetric galactic nuclei. They analyzed the depletion and refilling of loss cone orbits and found that tidal disruption rates could be increased by a moderate factor due to axisymmetry as compared to spherical symmetry. In their work chaotic orbits with low angular momentum, which can reach just outside the influence radius at apocenter, but also get close to the central SMBH at pericenter, cause some difficulty in comparison with Fokker-Planck models, as was already found by Malkov et al. (1993) (Note that the last author of this paper is the same person than the last author of Malkov et al. (1993), there was a mistake in retranslating the name from Russian language).

In this work we follow an experimental numerical approach to the problem, following Paper I for the case of spherically symmetric systems. We treat particle number and tidal radius as free parameters and analyze the tidal accretion rate of the system as a function of the strength of deviation from spherical symmetry. We measure the shape of the loss cone in axisymmetric potential and and characterize the characteristic orbits of stars in the loss cone. We find that it is indeed enlarged and can account for the higher TDR as compared to spherically symmetric galactic nuclei.

This paper is organized as follows: we describe the model setup of the simulation in Section 2 and present the result of TDR measurement in Section 3. Section 4 is devoted to the measurement of loss cone shape in axisymmetric potential and we demonstrate the enlargement of loss cone. In Section 5, we present the result for the origin and orbital classification of disrupted stars. In Section 6, we discuss the potential application of our results.

2. N-BODY MODEL

We adopt the standard N-body unit definitions from Heggie & Mathieu (1986), namely $G = M = 1$ and $E = -1/4$, where G is the gravitational constant, M is the total mass of the model cluster and E is the total energy. In our N-body models we assume that all the particles have the same mass, so $m = 1/N$, where m is the particle

mass and N is the total particle number. To preserve the scale invariance of our N-body simulations we fix the initial black hole mass relative to the total mass of the star cluster (0.01) and use the particle number and the tidal radius r_t in N-body units (which is a dimensionless number) as free parameters. We have shown in Paper I that the method of scaling to realistic parameters for N and r_t can be used to obtain astrophysically meaningful results from the collection of our models. In order to support our scaling procedure we even do not change the tidal radius during the simulations - since the BH mass changes within one order of magnitude only during the simulation, relative changes in tidal radius are small (notice that $r_t \propto (M_\bullet)^{1/3}$).

The initial distribution of particles follows a generalized King model with rotation. The distribution function is (Einsel & Spurzem 1999; Ernst et al. 2007)

$$f(E, J_z) = C \cdot [\exp(-\frac{\mathrm{E}}{\sigma_\mathrm{K}^2}) - 1] \cdot \exp(-\frac{\Omega_0 \mathrm{J_z}}{\sigma_\mathrm{K}^2}), \qquad (2)$$

where σ_K is the King velocity dispersion and Ω_0 is a characteristic angular velocity. Since we are considering an isolated system, the Φ_t is set to 0. This rotating King model has two dimensionless parameters: W_0 and ω_0. The King parameter $W_0 = -\Phi_0/\sigma_K^2$, where Φ_0 is the central potential, controls the degree of central concentration. And the rotation parameter $\omega_0 = \sqrt{9/(4\pi G\rho_0)} \cdot \Omega_0$, where ρ_0 is the central density, controls the degree of rotation. $\omega_0 = 0$ will reduce the model to a usual non-rotating spherically symmetric King model.

We limit our current study to only one concentration parameter $W_0 = 6$ and two rotation parameters $\omega_0 = 0.3, 0.6$; the density profile of King model with this concentration is similar to that of the Plummer model used in Paper I, so it is possible to compare with the previous results and focus on the effects of rotation and axial symmetry only. The rotation is moderate (cf. e.g. Einsel & Spurzem (1999)) and resembles that of Milky Way globular clusters.

For completeness we also employ non-rotating King model with $W_0 = 6$ and $\omega_0 = 0.0$, which is used as a fiducial model and also a bridge to the results of Paper I, confirming our claim that it indeed closely resembles the results for the Plummer model used in Paper I (e.g. in the evolution of the TDR). In another test run we used a larger rotation with $\omega_0 = 0.9$ - it experienced an unstable stage during which a bar formed but quickly disappeared. This bar formation could probably be identified with the radial orbit instability of Aguilar & Merritt (1990). We note that our standard models with $\omega_0 = 0.3, 0.6$ remain fully axisymmetric during the entire simulation; to study tidal disruption in triaxial systems with bars is beyond the scope of our current paper.

Fig. 1 shows the axial ratio (c/a) of the model clusters as a function of radius up to $r = 2.0$ (within which most of stars are located). We estimate the axial ratio for both rotating models, using the moment of inertia tensor measured in concentric shells. One can see c/a is close to 1 at the innermost part and decreases outward: $\omega_0 = 0.3$ model decreases slowly to its minimum value 0.9; $\omega_0 = 0.6$ model decreases faster and has a minimum value 0.71. If we measure the c/a for the whole cluster, the results for the two models are 0.9 ($\omega_0 = 0.3$) and 0.75 ($\omega_0 = 0.6$). Fig. 1 also shows that c/a is almost unchanged during long time evolution, except for the inner part of $\omega_0 = 0.6$ model, which exhibits slight decrease.

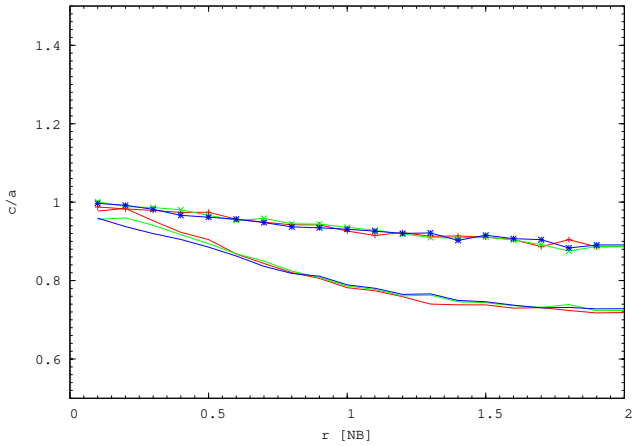

Figure 1. Axial ratio for rotating models as a function of radius. For each model we show the axial ratio measured at different evolution stage: T=0 (red); T=500 (green); T=1000 (blue). Lines with symbols are results for $\omega_0 = 0.3$ model, lines without symbols are for $\omega_0 = 0.6$ models.

In rotating systems, there is a phenomenon called gravo-gyro instability, which is caused by the negative specific moment of inertia (Inagaki & Hachisu 1978; Hachisu 1979, 1982). This kind of instability happens in long term evolution of rotating cluster which is much longer than our integration time (Ernst et al. 2007).

The model set is summarized in Table 1.

Table 1
Full set of our model runs.

Model	N/K	ω_0	r_t	T
R20w00	64	0.0	10^{-3}	1500
R30w00	128	0.0	10^{-3}	1600
R21w00	64	0.0	10^{-4}	1500
R31w00	128	0.0	10^{-4}	1300
R20w03	64	0.3	10^{-3}	1500
R30w03	128	0.3	10^{-3}	1500
R21w03	64	0.3	10^{-4}	2600
R31w03	128	0.3	10^{-4}	2000
R20w06	64	0.6	10^{-3}	1500
R30w06	128	0.6	10^{-3}	1500
R21w06	64	0.6	10^{-4}	1600
R31w06	128	0.6	10^{-4}	2000

Note. — Column 1 : Model codename. Column 2 : Particle number in the unit of K(=1024). Column 3 : dimensionless rotation parameter. Column 4 : black hole's tidal radius. Column 5 : total integration time. r_t and T are in model unit.

We run the simulation for more than one initial half-mass relaxation time (t_{rh}), which is estimated using the same formula in Paper I and the values can be found there as well (Table 2).

All simulations are running with the φGRAPE code (Berczik et al. 2011), which runs with high performance (up to 350 Gflop/s per GPU) on our GPU clusters in Beijing (NAOC/CAS). This code is a direct N-body sim-

ulation package, with a high order Hermite integration scheme and individual block time steps. A direct N-body code evaluates in principle all pairwise forces between the gravitating particles, and its computational complexity per crossing time scales asymptotically with N^2; however, it is *not* to be confused with a simple brute force shared time step code, due to the block time steps. We refer more interested readers to a general discussion about N-body codes and their implementation in Spurzem et al. (2011a,b). The present code is well tested and already used to obtain important results in our earlier large scale few million body simulation (Khan et al. 2012).

3. TIDAL DISRUPTION RATE (TDR)

3.1. *Results of our work*

In this section, we present the TDR measured in simulations with our rotating King models and compare it with the TDR of the non-rotating model of Paper I. In Fig. 2, we show the TDR (both in terms of mass and particle number) as it evolves with time for two different tidal radii; in each panel two different rotation parameters are plotted together with the data of the non-rotating system. The time is given in units of initial half mass relaxation time t_{rh}, which is convenient for comparison of simulations with different particle numbers. To smooth out fluctuations due to particle noise we have plotted in the figure the TDR averaged over a time interval (here $1/4t_{rh}$).

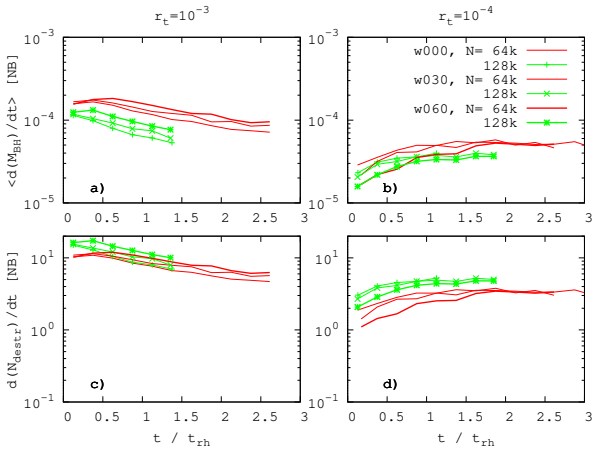

Figure 2. TDR as a function of time in units of initial half mass relaxation time; averaged over intervals of $1/4t_{rh}$. Top panels: mass accretion rate; bottom panels: particle accretion rate; left and right panels for two different tidal radii as indicated. Curves with symbols are stand for 128K models, those without symbols are stand for 64K models. Line thickness indicate different rotating parameters.

The TDR with a large tidal radius (i.e. $r_t = 10^{-3}$) initially quickly rises in the $N = 64K$ model to its peak value, and then decreases; for the $N = 128K$ model the TDR almost decreases from the beginning. The initial phase is connected with the formation of a central density cusp in the surrounding stellar system and with the process of transition from initially full to empty loss cone. The BH gains mass from the accreted stars, thus the mass ratio between stars and the BH ($\gamma := m/M_\bullet$) decreases with time, and as a result the BH's random motion damps. We have discussed in Paper I that the status of the loss-cone is connected with the BH's Brownian motion in the sense that once the amplitude of Brownian motion is smaller than $10r_t$ the system enters the empty loss-cone regime, during which the cusp and central density are still growing but TDR begins to fall. In the $N = 128K$ model, the mass ratio γ is smaller, so the initial loss cone depletion is very short, practically invisible in the plots, and the subsequent evolution is determined by cusp formation and damping of BH motion.

In the models with small tidal radius ($r_t = 10^{-4}$), there is always an initial growth phase of TDR, followed by the convergent approach to a stationary state. Due to the small r_t their BH growth is slow, thus they need more time to achieve the mass required to limit their Brownian motion.

Fig. 2 also shows the TDR dependence on rotation parameter ω_0 as a new result compared to Paper I. For large tidal radius ($r_t = 10^{-3}$), faster rotation will result in a higher TDR, note that these models are in empty loss-cone regime. Table 2 list out the numbers for TDR measurement. One can see $\omega_0 = 0.3$ model has a TDR on average 13 percent higher than $\omega_0 = 0.0$ model. And TDR in $\omega_0 = 0.6$ model is on average 35 percent higher than that in $\omega_0 = 0.0$ model. BH mass of these 3 models measured at $T = 1500$ are 0.131, 0.143 and 0.167. The fractional increase of final BH mass with increasing degree of rotation is consistent with the result of Fiestas et al. (2012). The reason for this dependence of ω_0 is that in these systems the effective loss-cone is larger than classic one in spherical system. We will investigate such an enlarged loss-cone in more detail in the next section. For small tidal radius ($r_t = 10^{-4}$), however, we observe a different behavior of TDR. From beginning to about $\sim 1.5t_{rh}$, faster rotation result in a smaller TDR! The argument presented by Magorrian & Tremaine (1999) may provide some hints: if BH's wandering time-scale is shorter than dynamical time-scale, a decrease in TDR will happen. We note in the simulation at this early stage the BH is quickly wandering due to its small mass and slow growth. Furthermore, in axisymmetric systems a star's pericenter distance changes with time (even ignoring irregular perturbations from other stars). So when the BH comes back to the place where it was, it may still miss the star which is supposed to be disrupted shortly before.

Table 2
TDR results for $r_t = 10^{-3}$ models.

t/t_{rh}	$\dot{N}_0$	$\dot{N}_3$	$\dot{N}_3/\dot{N}_0$	$\dot{N}_6$	$\dot{N}_6/\dot{N}_0$
0.25	14.96	15.41	1.03	16.30	1.09
0.50	12.89	13.67	1.06	17.30	1.34
0.75	10.44	12.07	1.16	14.52	1.39
1.00	8.73	10.32	1.18	12.65	1.45
1.25	7.97	9.73	1.22	11.09	1.39
1.50	6.99	7.93	1.13	10.04	1.44

Note. — Measured TDR for models with same N (128K) and r_t (10^{-3}) but different rotating parameters, at different evolution time. $\dot{N}_0$ is TDR in classic King model ($\omega_0 = 0$); $\dot{N}_3$ and $\dot{N}_6$ are results for $\omega_0 = 0.3$ and $\omega_0 = 0.6$ models. We also give the boost factor $\dot{N}_3/\dot{N}_0$ and $\dot{N}_6/\dot{N}_0$.

Afterwards the system begins to enter the empty loss cone regime, and all TDR curves converge to each other; for small tidal radius more tidally disrupted stars originate from inside the BH influence radius, where the system is approximately spherically symmetric. Any deviation from spherical symmetry in our rotating models prevails near and outside the influence radius. Convergence of TDR reflects the original results obtained in Paper I for spherical systems.

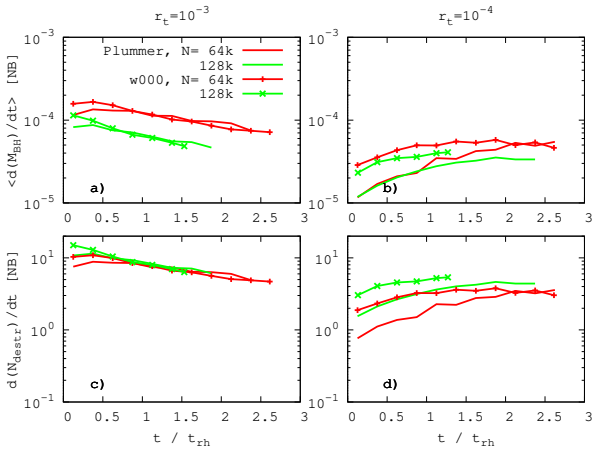

Figure 3. x axis is time in unit of initial half-mass relaxation time. y axis for panel a) and b) is the averaged mass accretion rate in given time range (i.e. $1/4\ t_{rh}$); y axis for panel c) and d) is the number accretion rate. Panel a) and c) show the result for $r_t = 10^{-3}$. Panel b) and d) show the result for $r_t = 10^{-4}$.

Fig. 3 compares the TDR of classic King model ($W = 6, \omega_0 = 0.0$) with that in Plummer model. In $r_t = 10^{-3}$ models, except the initial higher accretion rate in King model, the two models have similar TDR in following evolution. While in the case of $r_t = 10^{-4}$, King model have a higher accretion rate during most of the time, but later on they gradually come to the same level as the Plummer model. The higher rate in King model could be explained by the slightly higher density in the core region at beginning. In the following evolution of $r_t = 10^{-3}$ models, the two models form cusp similar to each other so they have roughly same accretion rate. In the case of $r_t = 10^{-4}$, the initial accretion rate ratio $\dot{N}_{King}/\dot{N}_{Plum}$ is higher than those in $r_t = 10^{-3}$. BH inside King cluster growing faster and also the growth of cusp, in the following evolution King model always have a higher density in the cusp which in return gives a higher accretion rate. Only after the BH gain enough mass and become a "static" object, the accretion rate slowly reaches a maximum and begins to drop afterward.

Up to this point, all results were presented in model units (N-body units). As in Paper I (see Sect. 5 and Appendix therein) we will discuss now any conclusions which can be made for the case of real galactic nuclei and environments from our results. This will be useful for observational programmes on TDR. To predict the TDR in real galactic nuclei, we use the method of scaling. The TDR obtained in our simulations has to be scaled up in two ways: first from relatively low ($N \sim 10^5$) to more realistic high particle numbers ($N \sim 10^8$). Second, our accretion radius r_t has been chosen very large compared to any realistic tidal radius (for smaller N simulations it has to be done in order to get any meaningful results on TDR). So, we also have to discuss how to scale down the TDR from our simulated values of r_t $(10^{-3}, 10^{-4})$ to the small more realistic regime of r_t (10^{-7}). This can be done by applying scaling relations from known scaling laws (obtained e.g. from Paper I and other literature) for N, and an empirically determined one for r_t. We have shown above that the TDR in King ($W_0 = 6$) and Plummer models is very similar, so we expect the scaling formula (A10) derived in Paper I for a Plummer model to be also valid for our King model used here. So, we apply the same boost factor of TDR with respect to the axisymmetry of a galactic nucleus for the real galactic nucleus as we find here in this paper for our simulated systems. For example, in Paper I we estimated the TDR of the Milky Way SMBH to be $1.09 \times 10^{-5}\mathrm{yr}^{-1}$ after a scaling procedure with respect to N and r_t. By fitting surface brightness profile to mid-infrared images of the nuclear cluster in our Milky Way, Schödel et al. (2014) reported the mean ratio between minor and major axes is 0.71, which is close to our rotating $\omega_0 = 0.6$ model. For this model we find a boost of TDR by 35% in our simulations, and we apply the same factor here for the case of axisymmetry, to get a higher TDR of $1.47 \times 10^{-5}\mathrm{yr}^{-1}$.

3.2. *Relation to other current papers in the field*

With regard to the enhancement of TDR in axisymmetric systems we have shown that our results are in agreement with Fiestas et al. (2012); but recently numerical simulations published by Vasiliev & Merritt (2013) and Vasiliev (2014) seem to contradict our findings. They claimed that the TDR in axisymmeric nuclei can be a few times larger than in the spherical case. Also Li et al. (2014) analyzed the distribution of stellar orbits in an axisymmetric galaxy and found that total number of stars that can interact with the central SMBH binary is six times larger than in the spherical system. In this subsection we will discuss why there is such a discrepancy to our results - we find a much smaller enhancement of TDR in axisymmetric systems.

The main difference between the cited papers and our work is the initial model. In all of the above mentioned papers, a flattened Dehnen model is used (their density profile, given the parameters they chose, is identical also to the Hernquist model). Their models possess a fixed axial ratio ($c/a = 0.75$) throughout the entire cluster and an initial central cusp, while our rotating initial model has initially a core density distribution in the center, and we have a radial variation of c/a from nearly spherical ($c/a \approx 1$) to about $c/a \approx 0.7$ in the outskirts (see Fig. 1). However, in the radius range where most of the disrupted stars originate from (c.f. Fig. 9), the system deviates significantly from spherical symmetry, thus we can confirm that the enhancement of TDR is connected with the non-spherical geometry. But in the relevant region of our $\omega_0 = 0.6$ deviation from spherical symmetry is less than in the other cited papers, which may be an explanation for the weaker effect in our case.

We also notice that even within the cited other papers there are some discrepancies in the results even for models with the same initial density profile. For exam-

ple, the enhancement of the number of accreted stars in Vasiliev & Merritt (2013) was smaller than 100% (see Table 2 in their paper), while Li et al. (2014) found a factor of six. On the other hand some of the models in Vasiliev & Merritt (2013) only show mild enhancement which is in the same level as ours. Another example comes from the debate about the "final parsec problem" in SMBH binary evolution. Based on their simulation results, Khan et al. (2013) claimed that the "final parsec problem" is not a problem in axisymmetric host galaxies, while Vasiliev et al. (2014) reached an opposite conclusion according to their simulation. We notice that both of these work employs similar flattened galaxies model, however, they used a different method to generate the initial model.

Vasiliev & Merritt (2013), Vasiliev (2014) and Vasiliev et al. (2014) utilized the orbital superposition method of (Schwarzschild 1979) to construct their model. On the other hand, Khan et al. (2013) and Li et al. (2014) used another method called "adiabatic squeeze technique" developed by Holley-Bockelmann et al. (2001). We notice that in the process of adiabatic squeeze, which contains a step which applies a slow and smooth velocity change on the stars in the z direction. This step may artificially reduce the energy and angular momentum of the stars in the model cluster. Although the radius and velocity vectors of the stars are rescaled after the squeeze, it is not clear how the rescaling affects the phase space distribution. Thus it might be possible that the process produces more stars of low energy and low angular momentum. Another evidence of a similar effect can be derived from Vasiliev (2014); while they still use the orbital superposition method they changed the generation of their initial model so that it creates more low energy and low angular momentum stars. In their test run (Fig. 2 in their paper) we see a much larger enhancement of the number of accreted stars compared to Vasiliev & Merritt (2013). So to add more low energy and angular momentum stars seems to be promising in abridging the different enhancement factors between Vasiliev & Merritt (2013) and Li et al. (2014). We suggest that a detailed comparison between models constructed with these two methods (and their phase space distribution) should be performed in order to explain the discrepancy.

According to Li et al. (2014) the central two parsecs of their model galaxy exhibit a slight triaxiality, which could also introduce some additional centrophilic orbits, thus increase the number of stars that can interact with the central SMBH binary.

Before finishing this section, we want to make a final remark on the result of Li et al. (2014). Their model integrates individual orbits in a fixed model potential with one SMBH in the center, in a static way. So the number of stars that can interact with the central SMBH binary according to their results should be considered as an upper limit. Once two-body relaxation is turned on, some of the stars that are supposed to be inside the loss cone might be scattered out. And the presence of a SMBH binary in an evolving system may also affect the result of how many stars can interact with them.

4. LOSS CONE IN AXISYMMETRIC POTENTIAL

First, we summarize the loss cone theory for stellar orbits in a spherically symmetric gravitational potential, in order to discuss different behavior in an axisymmetric potential later. If a stellar orbit has a pericenter distance less than the tidal radius it is considered to be in the loss cone. In spherical symmetry the boundary of the loss cone can be expressed in terms of a critical loss cone angular momentum $J_{lc} \approx \sqrt{2GM_\bullet r_t}$ (if $r \gg r_t$; cf. e.g. Amaro-Seoane et al. (2004)). The loss cone is then defined as the region in phase space where the angular momentum J of a star fulfils $J < J_{lc}$. All stars inside the loss cone will reach the tidal radius within a dynamical (orbit) time scale. As a consequence the loss cone would become empty in that relatively short time. Once a star is inside the loss cone and reaches the tidal radius, we assume that it will be destroyed by the BH's tidal force instantaneously and add its total mass to the black hole at the same moment. Most authors studying stellar dynamics and TDR of star clusters around a BH used similar approximations. Rees (1988) already argued that the stellar debris after tidal disruption will make several orbits until it is finally accreted by the BH; nevertheless the orbital time near the BH is very short compared to the original orbital time of the star before its disruption. Recent detailed simulations on tidal disruptions (Guillochon & Ramirez-Ruiz 2013; Hayasaki et al. 2013, 2015) show that in some case not all material of the star may be accreted and that general assumptions about the tidal fallback rate are not correct; for example in a longer lived accretion disk may form, which would delay the black hole growth. In a spherical system, without interactions between the stars, angular momentum $\mathbf{J}$ would be strictly conserved. So, without any repopulation of the loss cone, the accretion process would stop after a few dynamical times. But stars do interact with each other while moving inside the star cluster by two body relaxation through mutual encounters; in this process they can exchange angular momentum and energy and so the loss cone will be repopulated in the two body relaxation time scale, which is generally long compared to the dynamical time (Cohn & Kulsrud 1978; Amaro-Seoane et al. 2004). The repopulation of the loss cone is modelled in these papers as a diffusive process using the Fokker-Planck approximation.

In an axisymmetric potential, the situation is more complex since $\mathbf{J}$ is not a conserved quantity. It changes continuously due to the non-central force resulting from the geometry of the potential. In this case, stars with $J > J_{lc}$ may have a chance to drift into the loss-cone and get disrupted. In other words, the loss cone is enlarged in the J dimension in axisymmetric potential. However, the z component of angular momentum J_z is still conserved, so a solid boundary of the loss-cone is $J_z \leq J_{lc}$. Magorrian & Tremaine (1999) investigated this topic using a symplectic map introduced by Touma & Tremaine (1997). In this work, we analyze the enlarged loss cone in phase space in terms of energy E, modulus of angular momentum J and the z component of angular momentum J_z for stellar orbits near the BH. We use a different approach as Magorrian & Tremaine (1999) here, which is based on a numerical particle scattering experiment. In what follows, we first describe the method we used in this experiment, then present our results.

First step, we need to know the smooth gravi-

tational potential as a function of position without the fluctuations due to the discrete particle structure. We use a so-called self-consistent field code (SCF, Hernquist & Ostriker (1992)) to generate the analytical function for the gravitational potential. The expansion coefficients $C_{lm}, D_{lm}, E_{lm}, F_{lm}$ used in computing forces (Eq.(3.21)-(3.23) in Hernquist & Ostriker (1992)) are computed based on snapshot data generated during the direct N-body simulation. By default, the code uses radial basis functions labeled from $n = 0$ to $n_{max} = 14$, and spherical harmonic function truncated at $l_{max} = 10$.

Our particle distribution is self consistently achieved as a consequence of the co-evolution of stars and BH. Using the SCF code means that all two-body interactions are smoothed out in the experiment. Because we assume that most of the two-body interactions happens during the apocenter passage, which is also used in Touma & Tremaine (1997). After getting the coefficients, we can calculate the acceleration, jerk and do orbit integration using a Hermite 4^{th} integrator with variable time steps, developed by ourselves. This code works very well and the energy and angular momentum errors of the test particle stays in the level of 10^{-9} over long time integration. In an axisymmetric system all coefficient with $m \neq 0$ should be 0. But in practice one will get some small numbers very close to 0 due to particle noise. We just ignore these terms, otherwise J_z would no longer be conserved. We also ignore coefficients with odd l, because the rotating system should be symmetric about the equatorial plane and do not have pear-like shape.

Next step is to generate initial positions and velocities for test particles. The basic idea of this experiment is to do parameter space scanning. We uniformly sample E, J and J_z, all test particles are initially put at their apocenter. Firstly, we choose a particular energy and calculate J_{lc} through equation $J_{lc} = r_t\sqrt{2(\Phi(r_t) - E)}$. Then we choose a pair of (J, J_z), J can be a few times larger than J_{lc} but J_z keeps smaller than J_{lc}. Given the combination of (E, J, J_z) and the potential distribution we can find the apocenter position given by (r, θ). Here r is distance to center and θ is the angle between position vector and z-axis. We note that there are actually four parameters (E, J, J_z, θ) to define the initial conditions for a particular orbit. So we further sampled 100 data points in θ dimension. In order to plot the result in a 2D plane, we introduce a filling factor P for every (E, J, J_z) combination to describe this θ dependence, which is the fraction of stars in the loss cone for a given combination of (E, J, J_z) (number of data points in loss cone divided by total sample size, e.g. 100), meaning that among all stars with same (E, J, J_z) only a fraction of P are inside the loss cone.

By our definition a star in the loss cone will be disrupted by the BH within one dynamical time, so for every test particle we only integrate their orbits for one orbital cycle. If a particle comes back to its apocenter, we consider it as out of the loss cone and move to the next integration with new initial orbital data.

Fig. 4 shows results from the experiment in a slowly rotating model ($\omega_0 = 0.3$), it represents the loss cone shape in phase space. Since J is not conserved we use its initial value at apocenter for the figure; at the time

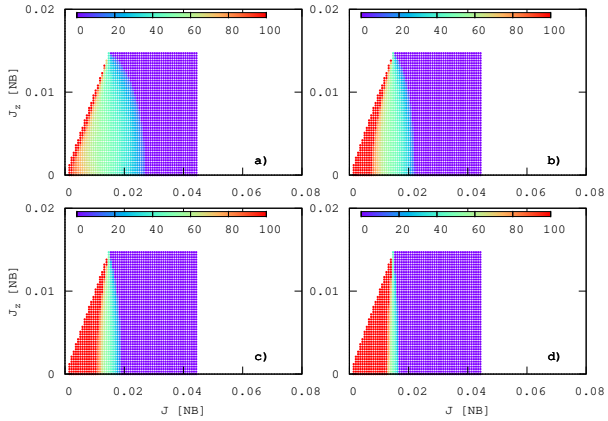

Figure 4. Filling factor P of the loss coneas a function of J and J_z for different energies; the x axis is the modulus of the total angular momentum J, while the y axis is its z component J_z. Panel a) correspond to $E = -1.3$, b) $E = -1.5$, c) $E = -1.7$, d) $E = -1.9$. Colors represent the filling factor P in percentage. All data are given in standard N-body units.

of disruption J must be less than J_{lc}. From panel a) to d), the energy of the test particles are in descending sequence, so their position of apocenters are getting closer and closer to central BH. One can see that the whole plane comprises 3 regions: 1) inner region where P equals 1, meaning particles with these (E, J, J_z) can hit the BH within one dynamical time scale; 2) transition region where P is non-zero but less than 1, particles with these (E, J, J_z) have a chance to hit the BH depending on their apocenter position (θ value); 3) outer region where $P = 0$, none of particle in this region can hit the BH. In panel a) one can see only a few points are red and a lot of points are located in transition region. From a) to d), the fraction of $P = 1$ points in the (J, J_z)-plane increases and the transition region is compressed by the inner and outer region in horizontal direction (J dimension). This is because test particles with high energy (loosely bound or unbound with respect to the BH) can go beyond the BH's influence radius to the intermediate and outer regions of the cluster, where the axisymmetric stellar potential dominates. The angular momentum of these test particles will have large variations. So a wide transition region exists in high energy cases. But in the low energy case (stars strongly bound to the BH), e.g. panel d), test particles are moving inside the BH's influence sphere where the potential is dominated by the BH and thus approaches spherical symmetry. All loss cone stars following the classical loss cone approximation, should have both J and J_z to be smaller than J_{lc}. In all panels of Fig. 4, on the contrary, we see how stars with $J > J_{lc}$ could be still in the new, extended loss cone of an axisymmetric system with a certain non-zero probability.

For faster rotating models ($\omega_0 = 0.6$) the results are similar. Three regions are presented on the (J, J_z) plane, however, the extent of each region is different from the counterpart of same energy in slow rotating model. Fig. 5 gives an example, in both left ($\omega_0 = 0.3$) and right ($\omega_0 = 0.6$) panel the test particle have same energy, however, the resulting appearances are quite different.

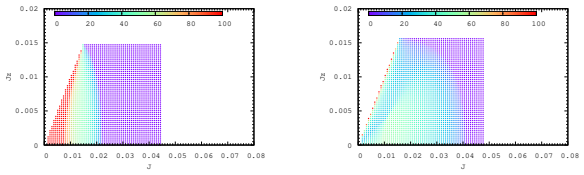

Figure 5. Comparison between 2 models with same test particle energy -1.5. x axis is module of angular momentum in N-body unit. y axis is z component of angular momentum. Left panel correspond to $\omega = 0.3$; right panel $\omega = 0.6$. Colors indicate the filling factor P in percentage.

In the left panel we see the the outer border extended to $J = 0.024$, while in the right one the outer border goes to $J = 0.04$ and is not as clear as that in the left panel. Also in the right panel the red region is almost disappeared. These results show how rotation modifies the loss cone shape in phase space. In both of these plots, the maximum radius stars can achieve are roughly the same. However, faster rotation means we have a more flattened cluster shape, which enhances the torque acting on stars, thus the variation in J becomes larger. So, the higher the degree of rotation in the stellar system, the larger is the extension of the loss cone in J direction.

On first glance at Fig. 4 (also Fig. 5) one might think that the loss cone is generally enlarged by a significant factor. However, as we pointed out above, there is a filling factor P for every point on the (J, J_z) plane. To find the net enlargement of the loss cone in axisymmetric potentials we introduce an effective area S of the loss cone in these plots by integrating the filling factor P over the (J, J_z) plane. For example, the effective area of the classical loss cone is just given by the size of the triangle $J, J_z < J_{lc}$ in our plots, since in the classical case P is unity everywhere in this triangle region.

Now we compare the loss-cone size comparing the integrals S with each other. We define the quotient $\alpha_{lc} = S_{eff}/S_{lc}$, where $S_{lc} = J_{lc}^2/2$ is the classical loss cone integral. α_{lc} is plotted in Fig. 6 as a function of binding energy $|E|$. In the plot we show both slow and fast rotating models at two different evolution times. For the slow rotating model the ratio α_{lc} is even smaller than unity for binding energies larger than 1.4 - 1.5, meaning that at large $|E|$ the loss cone is smaller compared to the classical one. This is caused by the reduction of the probability P at the boundary and inside the classical loss cone region $J \leq J_{lc}$. P is decreasing from inside toward outside. While for intermediate $|E|$ case, although P is still decreasing function of J, the large number of valid points overwhelms, so the net effect is increasing the effective area. However, if one goes further toward small $|E|$ the ratio will drop again, like the case of fast rotating model. This is just because P is sufficiently small in this case and win the game. For fast rotating model, another interesting feature is the ratio drops below 1 at $|E| = 1.8$. From this figure we see that the enlargement of loss cone, quantified by the ratio α_{lc} as a function of binding energy. Interestingly, the change of the effective loss cone size in every energy slice is less than 5-10%. These mild changes seem unable to raise TDR with the amount observed in the simulation, to address this it will be useful if we can estimate the TDR based on the effective loss cone measurement and compare with simulation. However, the knowledge of how stars are distributed in energy and angular momentum is required. With the limited particle numbers of the model cluster, it is difficult to get an accurate and reliable distribution function. Also in current work, we sample the energy space with large intervals ($\Delta E = 0.1$), which may cause large errors in the estimated TDR. So we did not make the estimation. There are still plenty of works could be done with this topic.

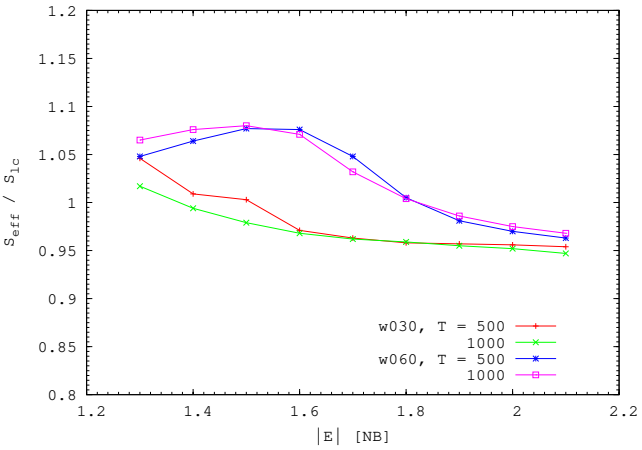

Figure 6. Ratio between effective area S_{eff} of loss-cone in axisymmetric system and S_{lc} in spherical system.

5. ORBITAL PROPERTIES OF DISRUPTED STARS

In this section, we investigate the origin of disrupted stars. Under the assumption that stars in loss cone can survive for only one orbital period, the origin of these stars can be examined by looking at their energy and angular momentum, as well as their origin (apocenter) in spatial coordinates (radius and angle θ). In spherical systems one can use effective potential to compute the apocenter of orbit, but in the axisymmetric case we do not have such convenient solutions except to run the simulation twice. In the first run we find out the ID for those stars that will be disrupted by BH. Then, in the second run we make records for these stars more frequently than other stars, in order to catch their last apocenter position.

We found in the beginning that the total TDR, especially for small r_t does only marginally depend on the rotation of the system; consistent with this we found in the previous chapter that the loss cone structure does change significantly, but the total integral over the loss cone space for axisymmetric systems yields only relatively small changes. Still it is interesting to study how the orbital properties of stars, which are tidally disrupted, change with the rotation of the system. In order to address this, we now turn back to our full N body simulations and study the distribution of $|E|$ (Fig. 7) and J (Fig. 8) of the disrupted stars at their apocenter passage in three time intervals. From Fig. 7 one can see that most of the tidally disrupted stars have a binding energy between 1 and 2, coincident with the small bumps in Fig. 6 where $\alpha_{lc} > 1$. Another evidence comes from

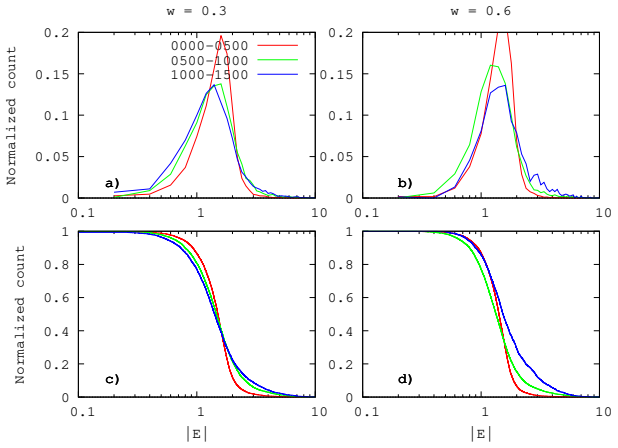

Figure 7. Panel a) and b) show normalized distribution of binding energy $|E|$ of tidally disrupted stars, for different rotating models and for three different time intervals (indicated by color) in the full N-body simulation with $r_t = 10^{-3}$. The distribution is normalized to the total number of disrupted stars in each time interval. Panel c) and d) show cumulative fraction profile corresponding to a) and b), respectively.

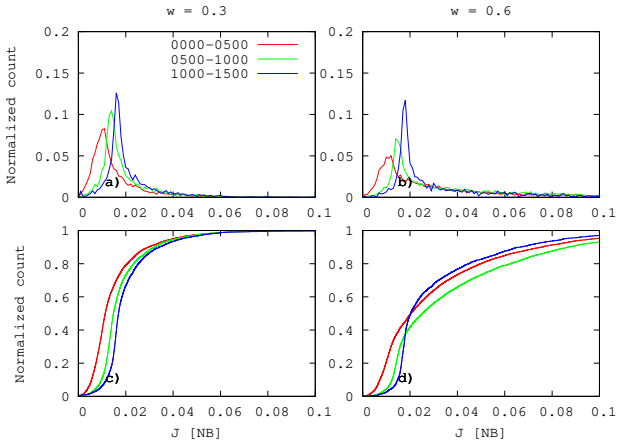

Figure 8. Same as Fig. 7, but here for the distribution of total angular momentum of the disrupted stars.

the distribution of J as shown in Fig. 8, where one can see the peaks are lying outside of the J_{lc} which is roughly 0.015. The peaks are moving toward larger J, which is caused by the increase of BH mass (recall the expression for J_{lc}). A significant fraction of stars comes from places outside of the classical loss cone in (J, J_z) plane.

In spherical systems it is usually sufficient to describe the apocenter of an orbit by its radial distance from the center (the BH); the orientation of the orbit does not play any role for the orbital time and the nature of the encounter with the central BH. However, in axisymmetric systems, orbits with different angle θ (the angle between position vector of the star at apocenter and the z-axis) will differ from each other significantly. Therefore we have to describe the distribution of apocenters of tidally disrupted stars in terms of both the r (Fig. 9) and θ (Fig. 10) dimension. From Fig. 9 one can see the peaks are quite far from the BH, in a region comparable to the BH influence radius, which is similar to the apocenter

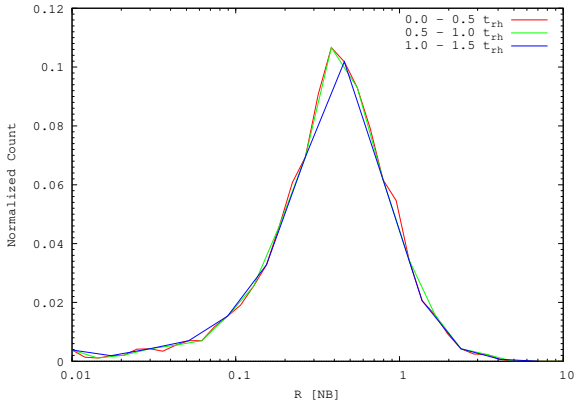

Figure 9. Distribution of last apocenter distance of disrupted stars in 3 different time interval. Each curve are normalized to the total number of disrupted stars in given time interval.

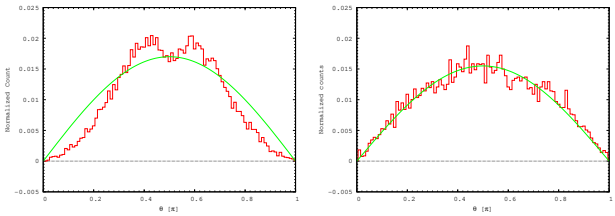

Figure 10. Normalized distribution of zenith angle θ of last apocenter of disrupted stars. Left panel is axisymmetric model, right panel is spherical model.

distribution in spherical systems (Paper I). The difference turns out to be in the θ dimension, as shown in Fig. 10. We compare the θ distribution between spherical and axisymmetric systems. Imagine we project all the apocenter points onto a sphere with radii equals 1. The measured number counts in each θ bin $\Delta N(\theta)$ are computed by $2\pi \cdot \Sigma(\theta) \cdot \sin(\theta)\Delta\theta$, where $\Sigma(\theta)$ is the surface density of projected points on the unit sphere. If apocenters are uniformly distributed with θ, $\Sigma(\theta)$ is constant, then $\Delta N(\theta) \propto \sin(\theta)\Delta\theta$. Here we choose an equal bin size, so the measured number count should follow a $\sin(\theta)$ curve. The right panel of Fig. 10 plots θ distribution for spherical model, which is taken from our last work (Paper I). In left panel we see the last apocenter distribution have deficit at polar region comparing to $\sin(\theta)$ curve, and excess at places beyond and below the equatorial plane, showing a double peak feature. The deficit at the polar region may have something to do with the flattening of the cluster, however, this is not the only reason. The double peak feature around the equatorial plane obviously does not relate to a geometrical origin, otherwise the peak should be placed at the equatorial plane. In Fig. 11 we compare the θ distribution between slow and fast rotating models. One can see that in fast rotating model, the double peaks are more significant, accompanied by a further deficit in the angle range $0.2 - 0.4\pi$ and $0.6 - 0.8\pi$.

In order to understand the double peak feature, we turn to the orbit structure of these disrupted stars. In non-spherical symmetric stellar system with a SMBH in its center, the space populated by stars can be divided into three parts depending on the distance to

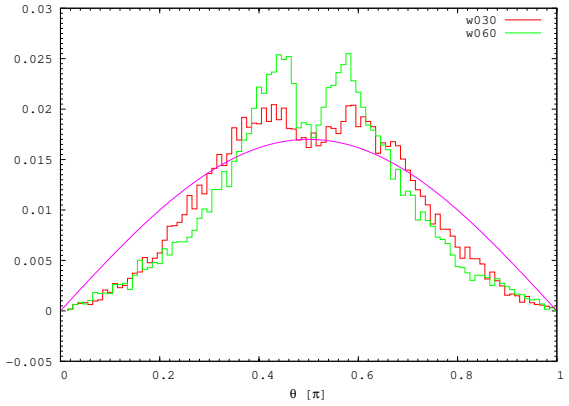

Figure 11. Normalized distribution of zenith angle θ of last apocenter of disrupted stars. Compare between slow (w030) and fast (w060) rotating models.

the BH, namely the regular, chaotic and mixing region (Poon & Merritt 2001). Inside the BH's influence radius r_h, the potential felt by the star is dominated by the BH plus a small perturbation from the non-spherical stellar potential. In this region, the motion of stars is essentially regular, as in a spherical potential. Outside of r_h, stars passing the center will suffer a large angle deflection by the BH, which in conjunction with the non-spherical potential near and outside r_h, could make their orbits stochastic.

We are interested in stellar orbits in an axisymmetric stellar potential, which can get close to the central BH. These are typically two classes of orbits, short-axis tube (SAT) and saucer (see Vasiliev (2014) for example); they can be distinguished by their third integral of motion I_3. Although I_3 may help us quickly distinguish orbit families, finding the functional form of I_3 is difficult (see Lupton & Gunn (1987) and discussion in Sridhar & Touma (1999)) and is beyond the scope of this paper. We choose alternative ways to do orbit classification, such as Surface of Section (SoS) plot and Fourier analysis of J_x (see Appendix).

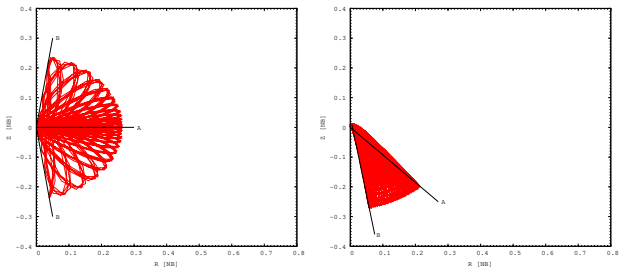

Figure 12. Examples of orbital structure for SAT (left) and saucer (right) orbit. Stars achieve maximum J when their instant orbital plane coincide with **B** plane, while minimum when coincide with **A** plane.

Fig. 12 gives examples of SAT and saucer orbits in configuration space. The plot is made in cylindrical coordinates so that one can catch the main point easily. For SAT orbit, one can see its apocenter can go both above and below the equatorial plane. While apocenter of saucer orbit can only exist on one side of mid-plane, due to restrictions by the 3rd integral. We also check the value of J at each apocenter passage. We find that SAT orbit achieve its minimum J at the equatorial plane; a saucer orbit cannot reach the equatorial plane, but its minimum J is achieved at the place which is next to the equatorial plane as marked in the plot by **A** plane. Recall in the last section we said no matter what J one star has at the apocenter, at the time of disruption it must be smaller than J_{lc}. So the last apocenter place should be around the **A** plane. This seems to be promising to explain the double peak in θ distribution, however, need to be confirmed. In order to see this we try to do orbit classification for the disrupted stars, which is computationally expensive. So we just randomly select a subsample of disrupted stars and divide them into 3 orbit families: SAT, saucer and others (here "others" means they do not belong to the former two families, and may be chaotic orbits). Among the 2943 sample stars, 1719 are classified as "others", 757 as saucer and 467 as SAT. Then we re-plot the r and θ distribution for different orbit families in Fig. 13.

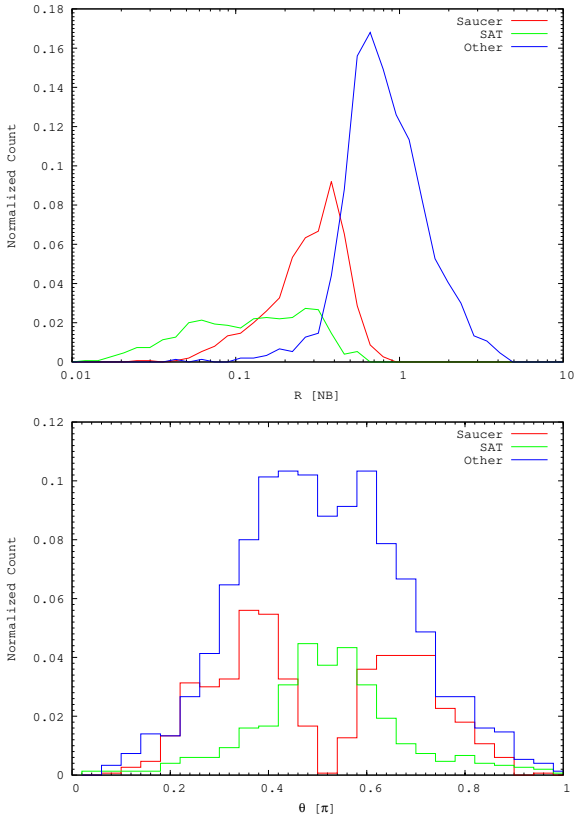

Figure 13. Normalized distribution of apocenter distance r and zenith angle θ of last apocenter of disrupted stars for different orbit families. The distribution is normalized to the number of stars in each orbit family.

The results show that the apocenter distribution of different orbit families not only differs in θ but also in r. One can see the innermost region is dominated by SAT orbits, and concentrated to the equatorial plane. Intermediate radius is mostly occupied by saucer orbits, and the distribution in θ shows double peaks as expected. Further out is the region dominated by orbits marked

as others. These orbits can go outside of the influence radius and are basically chaotic orbits. From Fig. 13 one can also find out the fractions of each orbit family contributing to the budget of disrupted stars: the largest fraction comes from chaotic orbits; SAT orbits contribute least to the budget because they are deeply buried in the cluster center where the total star number is small; the intermediate contribution is from saucer orbits which create the two peaks in the θ distribution.

6. CONCLUSIONS AND DISCUSSIONS

Tidal Disruption (TD) of stars by supermassive central black holes (SMBH) from dense rotating star clusters is modelled by high-accuracy direct N-body simulation. As in a previous paper on spherical star clusters we study the time evolution of the stellar tidal disruption rate and the origin of tidally disrupted stars, now according to several classes of orbits which only occur in rotating axisymmetric systems (short axis tube and saucer). In empty loss cone regime, comparing spherically symmetric and axisymmetric systems we find a higher TD rate in large r_t models in axisymmetric case, but for small r_t case - somewhat surprisingly - there is virtually no difference in the TD rate, maybe a small increase due to axisymmetry.

We define an extended loss cone by the condition that stars in the axisymmetric potential reach the BH within one orbit. A detailed analysis shows that the structure of the loss cone significantly differs from the spherical case; if J_{lc} is the critical angular momentum to be in the loss cone in a spherical system, and J, J_z are the total and z-component of the angular momentum of a stellar orbit, there are many stars with $J > J_{lc}$ in the loss cone; since, however, there are also some stars with $J > J_{lc}$, which are now **not** in the loss cone. In the total balance the number of loss cone stars is only very moderately increased.

In the experiment of measuring the shape of loss cone, we assume the test star can survive only one dynamical time in collisional system, after one orbit it will be "kicked" to another place in phase space due to interactions with other stars. However, in collisionless limit, if we allow the test star to survive more orbit cycles, test star with much higher J will also have chance to get rid of its angular momentum and be disrupted by BH. Then it is possible that an even larger loss cone region in phase space than what we presented here may exist, and result in a higher TDR. In order to check this, simulations with much more particles are needed and we would like to leave this task for future work.

The orbit type of disrupted stars strongly depends on energy as we discuss in detail in the previous sections. TD of stars most strongly bound to the BH are dominated by short-axis tube (SAT) orbits. In intermediate regions saucer orbits dominate, which create a characteristic double peak structure in the last apocenter position of their orbit relative to the equatorial plane. And further out chaotic orbits.

It is known for almost half a century that tidal disruption of stars should occur near SMBH, but only much more recently the X-ray emission of tidal disruption events has been detected (Komossa 2002; Komossa & Merritt 2008). A simple argument on the fallback time for tidal debris by Rees (1988) has led to the prediction of a characteristic power law of the light curve with time, which can be used to distinguish TD events from other transients. It is interesting that a SMBH binary can cause characteristic disruptions in such an otherwise standard TD light curve (Liu et al. 2014). Hayasaki and collaborators claim that eccentric TD events lead to somewhat longer lived central accretion disks (Hayasaki et al. 2013, 2015). It will be very interesting to see whether and how the evolution of tidal debris and the fallback rate are affected by different orbits of the disrupted stars as discussed here.

It has been claimed that rotation may help to quickly refill loss cones around binary supermassive black holes, which helps significantly to accelerate shrinking and final coalescence of SMBH binaries in cosmologically short time scales (Berczik et al. 2006; Preto et al. 2011; Khan et al. 2013; Khan 2014). In our paper we study by direct N-body simulation the tidal accretion of stars and their orbital parameters in rotating axisymmetric systems. We confirm the result of Vasiliev & Merritt (2013) that there is an increase in the rate of refilling of the loss cone, but it is moderate. However, the situation deserves more detailed study, because a SMBH binary creates a much stronger deviation from spherical symmetry than the one used in our models with single SMBH. And second the detailed structure of the rotation in a central nuclear star cluster could affect the enhancement of the loss cone.

ACKNOWLEDGEMENTS

We acknowledge support by Chinese Academy of Sciences through the Silk Road Project at NAOC, through the Chinese Academy of Sciences Visiting Professorship for Senior International Scientists, Grant Number 2009S1-5 (RS), and through the "Qianren" special foreign experts program of China.

The special GPU accelerated supercomputer laohu at the Center of Information and Computing at National Astronomical Observatories, Chinese Academy of Sciences, funded by Ministry of Finance of People's Republic of China under the grant ZDY Z2008-2, has been used for the simulations.

PB acknowledge the special support by the NAS Ukraine under the Main Astronomical Observatory GPU/GRID computing cluster project.

SZ thank Yohai Meiron for providing the SCF source code which is used in this work.

APPENDIX

ORBIT CLASSIFICATION

Surface of Section

From Fig. 14 we can see the whole accessible region on (R, v_R) plane is divided into two parts (note that points with opposite v_R actually belongs to same orbit, so this plot is symmetric with horizontal axis). Each part represents a family of orbit. Curves that intersect with R-axis are footprints of short axis tube (SAT) orbits, others are of saucer orbits.

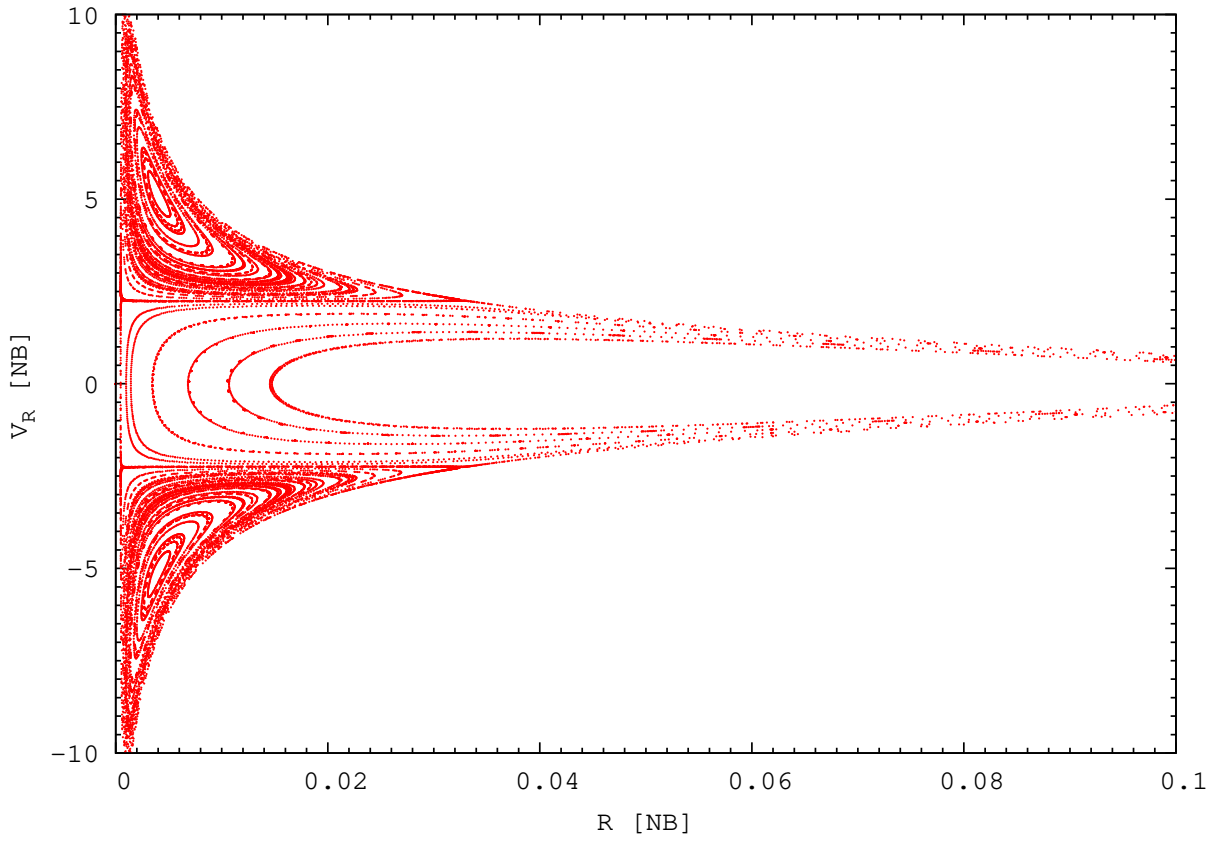

Figure 14. Surface of section plot. x axis is distance R to origin on equatorial plane. y axis is $v_R \equiv dR/dt$ when star go across the equatorial plane.

Fourier Analysis of J_x evolution

In axisymmetric potential, force is not centripetal hence exerted a torque on the star which will change the x and y components of its angular momentum. Fig 15 show the time evolution of J_x for both SAT and saucer orbits. The pattern of J_x and J_y are the same but shifted with a phase of $\pi/2$, so in the following discussion we only focus on J_x. Furthermore, the evolution of J_x shows some quasi-periodicity. From eye inspection, one can guess the mathematical expressions for the curves.

As shown in Fig. 15, the curve for SAT orbits seems to be represented by $\sin(\mathrm{f_1 t})(1 + \cos(\mathrm{f_2 t}))$ ($\mathrm{f_1} < \mathrm{f_2}$), which can be further converted to $\sin(\mathrm{f_a t}) + \sin(\mathrm{f_b t}) + \sin(\mathrm{f_c t})$ (ignore coefficients before the trigonometric functions), with $\mathrm{f_a} = \mathrm{f_1}, \mathrm{f_b} = \mathrm{f_2} - \mathrm{f_1}$ and $\mathrm{f_c} = \mathrm{f_2} + \mathrm{f_1}$. If we perform a Fourier analysis on this curve, we expect to find 3 principal frequencies: $\mathrm{f_a}, \mathrm{f_b}, \mathrm{f_c}$ in ascending sequence. And these 3 frequencies satisfy the equation $\mathrm{f_a} = (\mathrm{f_c} - \mathrm{f_b})/2$.

For saucer orbits, the curve seems to be represented by $\sin(\mathrm{f_1 t})\cos(\mathrm{f_2 t})$ ($\mathrm{f_1} < \mathrm{f_2}$), following the same procedure we expected to find 2 principal frequencies: $\mathrm{f_a}, \mathrm{f_b}$, with $\mathrm{f_a} = \mathrm{f_2} - \mathrm{f_1}$ and $\mathrm{f_b} = \mathrm{f_2} + \mathrm{f_1}$.

A demonstration is shown in Fig. 16, one can clearly see the 3 principal frequencies for SAT orbits and the 2 for saucer orbits. Some of the small peaks appeared at higher frequencies which is the order harmonics and some are produced from other components.

We use both methods to cross check the validity of orbit classification for the tidally disrupted stars.

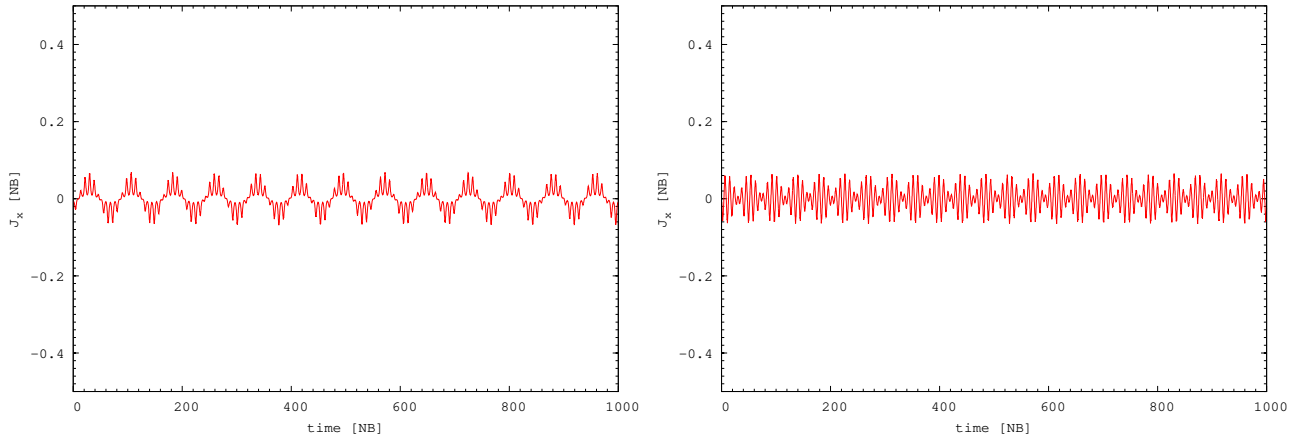

Figure 15. Time evolution of J_x for SAT orbit (left) and saucer orbit (right).

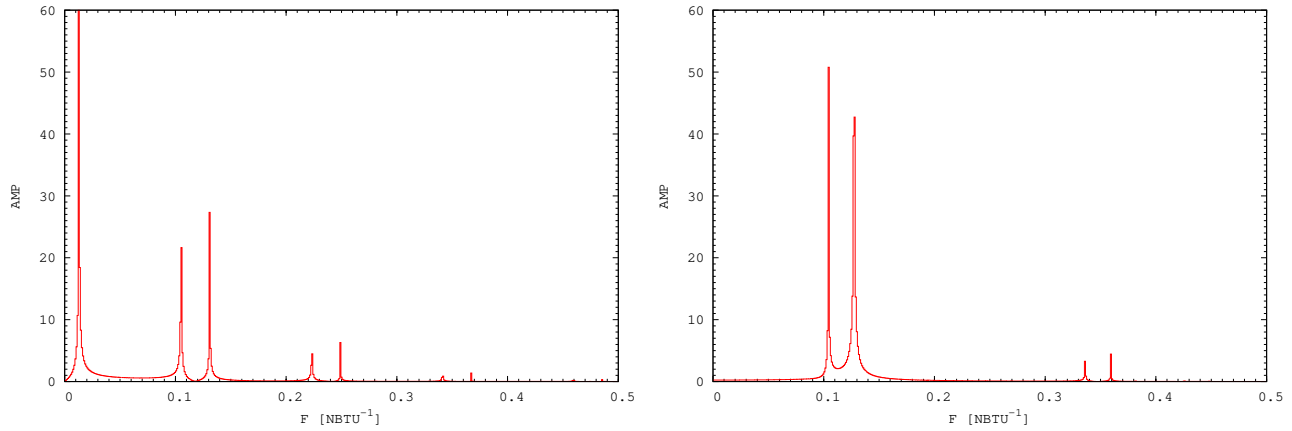

Figure 16. Fourier frequency distribution of J_x. Horizontal axis is frequency in unit of $[T]^{-1}$. Vertical axis is amplitude of corresponding component. Left panel represents SAT orbit, right panel represents saucer orbit.

REFERENCES

Aguilar, L. A. & Merritt, D. 1990, ApJ, 354, 33
Amaro-Seoane, P., Freitag, M., & Spurzem, R. 2004, MNRAS, 352, 655
Antonini, F., Capuzzo-Dolcetta, R., Mastrobuono-Battisti, A., & Merritt, D. 2012, ApJ, 750, 111
Berczik, P., Merritt, D., Spurzem, R., & Bischof, H.-P. 2006, ApJ, 642, L21
Berczik, P., Nitadori, K., Zhong, S., Spurzem, R., Hamada, T., Wang, X., Berentzen, I., Veles, A., & Ge, W. 2011, in International conference on High Performance Computing, Kyiv, Ukraine, October 8-10, 2011., p. 8-18, 8–18
Bois, M., Emsellem, E., Bournaud, F., Alatalo, K., Blitz, L., Bureau, M., Cappellari, M., Davies, R. L., Davis, T. A., de Zeeuw, P. T., Duc, P.-A., Khochfar, S., Krajnović, D., Kuntschner, H., Lablanche, P.-Y., McDermid, R. M., Morganti, R., Naab, T., Oosterloo, T., Sarzi, M., Scott, N., Serra, P., Weijmans, A.-M., & Young, L. M. 2013, in Astronomical Society of the Pacific Conference Series, Vol. 477, Galaxy Mergers in an Evolving Universe, ed. W.-H. Sun, C. K. Xu, N. Z. Scoville, & D. B. Sanders, 97
Böker, T., Laine, S., van der Marel, R. P., Sarzi, M., Rix, H.-W., Ho, L. C., & Shields, J. C. 2002, AJ, 123, 1389
Böker, T., Sarzi, M., McLaughlin, D. E., van der Marel, R. P., Rix, H.-W., Ho, L. C., & Shields, J. C. 2004, AJ, 127, 105
Cohn, H. & Kulsrud, R. M. 1978, ApJ, 226, 1087
Einsel, C. & Spurzem, R. 1999, MNRAS, 302, 81
Ernst, A., Glaschke, P., Fiestas, J., Just, A., & Spurzem, R. 2007, MNRAS, 377, 465
Evans, C. R. & Kochanek, C. S. 1989, ApJ, 346, L13
Feldmeier, A., Neumayer, N., Seth, A., Schödel, R., Lützgendorf, N., de Zeeuw, P. T., Kissler-Patig, M., Nishiyama, S., & Walcher, C. J. 2014, A&A, 570, A2
Fiestas, J., Porth, O., Berczik, P., & Spurzem, R. 2012, MNRAS, 419, 57
Fiestas, J. & Spurzem, R. 2010, MNRAS, 405, 194
Frank, J. & Rees, M. J. 1976, MNRAS, 176, 633
Greenhill, L. J., Henkel, C., Becker, R., Wilson, T. L., & Wouterloot, J. G. A. 1995, A&A, 304, 21
Gualandris, A. & Merritt, D. 2012, ApJ, 744, 74
Guillochon, J. & Ramirez-Ruiz, E. 2013, ApJ, 767, 25
Hachisu, I. 1979, PASJ, 31, 523
—. 1982, PASJ, 34, 313
Hayasaki, K., Stone, N., & Loeb, A. 2013, MNRAS, 434, 909
Hayasaki, K., Stone, N. C., & Loeb, A. 2015, ArXiv e-prints
Heggie, D. C. & Mathieu, R. D. 1986, in Lecture Notes in Physics, Berlin Springer Verlag, Vol. 267, The Use of Supercomputers in Stellar Dynamics, ed. P. Hut & S. L. W. McMillan, 233
Hernquist, L. & Ostriker, J. P. 1992, ApJ, 386, 375

Holley-Bockelmann, K., Mihos, J. C., Sigurdsson, S., & Hernquist, L. 2001, ApJ, 549, 862
Inagaki, S. & Hachisu, I. 1978, PASJ, 30, 39
Khan, F. M. 2014, in COSPAR Meeting, Vol. 40, 40th COSPAR Scientific Assembly. Held 2-10 August 2014, in Moscow, Russia, Abstract E1.20-5-14., 1462
Khan, F. M., Berentzen, I., Berczik, P., Just, A., Mayer, L., Nitadori, K., & Callegari, S. 2012, ApJ, 756, 30
Khan, F. M., Holley-Bockelmann, K., Berczik, P., & Just, A. 2013, ApJ, 773, 100
Khan, F. M., Just, A., & Merritt, D. 2011, ApJ, 732, 89
Kim, E., Einsel, C., Lee, H. M., Spurzem, R., & Lee, M. G. 2002, MNRAS, 334, 310
Komossa, S. 2002, in Reviews in Modern Astronomy, Vol. 15, Reviews in Modern Astronomy, ed. R. E. Schielicke, 27
Komossa, S. & Merritt, D. 2008, ApJ, 683, L21
Li, B., Holley-Bockelmann, K., & Khan, F. 2014, ArXiv e-prints
Lightman, A. P. & Shapiro, S. L. 1977, ApJ, 211, 244
Liu, F. K., Li, S., & Komossa, S. 2014, ApJ, 786, 103
Lotz, J. M., Telford, R., Ferguson, H. C., Miller, B. W., Stiavelli, M., & Mack, J. 2001, ApJ, 552, 572
Lupton, R. H. & Gunn, J. E. 1987, AJ, 93, 1106
Magorrian, J. & Tremaine, S. 1999, MNRAS, 309, 447
Malkov, E. A., Vil'Koviskij, E. Y., Nuzhnova, T. N., & Shpurtsem, R. 1993, in Problems of Physics of Stars and Extragalactic Astronomy, ed. A. V. Kurchakov, 139–152
Merritt, D. & Poon, M. Y. 2004, ApJ, 606, 788
Milosavljević, M. 2004, ApJ, 605, L13
Miyoshi, M., Moran, J., Herrnstein, J., Greenhill, L., Nakai, N., Diamond, P., & Inoue, M. 1995, Nature, 373, 127
Neufeld, D. A. & Maloney, P. R. 1995, ApJ, 447, L17
Poon, M. Y. & Merritt, D. 2001, ApJ, 549, 192
Preto, M., Berentzen, I., Berczik, P., & Spurzem, R. 2011, ApJ, 732, L26
Rees, M. J. 1988, Nature, 333, 523
Schödel, R., Feldmeier, A., Kunneriath, D., Stolovy, S., Neumayer, N., Amaro-Seoane, P., & Nishiyama, S. 2014, A&A, 566, A47
Schwarzschild, M. 1979, ApJ, 232, 236
Seth, A. C., Blum, R. D., Bastian, N., Caldwell, N., & Debattista, V. P. 2008, ApJ, 687, 997
Seth, A. C., Dalcanton, J. J., Hodge, P. W., & Debattista, V. P. 2006, AJ, 132, 2539
Spurzem, R., Berczik, P., Berentzen, I., Ge, W., Wang, X., Schive, H.-Y., Nitadori, K., & Hamada, T. 2011a, in Large Scale Computing Techniques for Complex Systems and Simulations, ed. W. Dubitzky, K. Kurowski, & B. Schott, Wiley Publishers, 35–58
Spurzem, R., Berczik, P., Hamada, T., Nitadori, K., Marcus, G., Kugel, A., Männer, R., Berentzen, I., Fiestas, J., Banerjee, R., & Klessen, R. 2011b, Computer Science - Research and Development (CSRD), 26, 145
Sridhar, S. & Touma, J. 1999, MNRAS, 303, 483
Touma, J. & Tremaine, S. 1997, MNRAS, 292, 905
Tremaine, S. D., Ostriker, J. P., & Spitzer, Jr., L. 1975, ApJ, 196, 407
Vasiliev, E. 2014, Classical and Quantum Gravity, 31, 244002
Vasiliev, E., Antonini, F., & Merritt, D. 2014, ApJ, 785, 163
Vasiliev, E. & Merritt, D. 2013, ApJ, 774, 87
Wang, J. & Merritt, D. 2004, ApJ, 600, 149
Zhong, S., Berczik, P., & Spurzem, R. 2014, ApJ, 792, 137